nature photonics

Supplementary information

https://doi.org/10.1038/s41566-024-01451-w

Coherently amplified ultrafast imaging using a free-electron interferometer

In the format provided by the authors and unedited

Table of Contents

1 Image acquisition

The electron microscope images presented throughout the manuscript were acquired using a direct-detection camera (K2 Summit, Gatan Inc.) mounted on the EELS instrument. To enable a direct comparison between measurements carried using one-point and two-points of interaction, the sum of the exposure times of all the phase-scan images (21 × 20 s) matched the exposure time of the conventional PINEM image (420 s).

In all the acquired images, there exist several detector-related sources of noise. As a result, the detector software usually performs substantial automated image processing on the raw image data. However, to achieve better control of the data analysis, we have exported the raw data and performed all the image processing ourselves.

2 Simulating phonon-polariton dynamics

In this section, we present the modeling of the phonon-polaritons (PhP) and their excitation by a laser pulse used in our simulations. We assume the laser excites multiple electric dipoles on the circular edges of the sample, with the relative phase and orientation of each dipole following the laser's polarization and propagation direction. We then find the PhP electric field pattern each dipole creates using the dyadic Green's function of a 45-nm-thick hBN sheet and assuming scattering boundary conditions.

For convenience, we set our axes with respect to the micro-drum such that the *z*-axis is the hBN surface normal. We consider a single-frequency plane wave exciting a set of dipoles along the edge of the sample. The incoming plane wave has the following electric field:

$$\boldsymbol{E}_{\mathrm{in}}(\boldsymbol{r},\omega) = E_0\big(\cos(\alpha)\,\hat{\boldsymbol{\varepsilon}}_{\boldsymbol{1}} + e^{i\beta}\sin(\alpha)\,\hat{\boldsymbol{\varepsilon}}_{\boldsymbol{2}}\big)e^{-i\frac{\omega}{c}(\sin(\theta)\cos(\varphi)x+\sin(\theta)\sin(\varphi)y-\cos(\theta)z)}, \quad (1)$$

where θ (φ) is the propagation angle with respect to the *z* (*x*) axis. The polarizations are $\hat{\boldsymbol{\varepsilon}}_{\boldsymbol{1}} = \sin(\varphi)\,\hat{\boldsymbol{x}} - \cos(\varphi)\,\hat{\boldsymbol{y}}$ and $\hat{\boldsymbol{\varepsilon}}_{\boldsymbol{2}} = \cos(\theta)\cos(\varphi)\,\hat{\boldsymbol{x}} + \cos(\theta)\sin(\varphi)\,\hat{\boldsymbol{y}} + \sin(\theta)\,\hat{\boldsymbol{z}}$. We note that the phase and polarization of the field break the circular symmetry in our simulations, which allows the center of the resulting PhP wave to move from the center of the sample. Notably, these polarizations cannot be addressed completely as TE and TM since there is no translational symmetry in any of the directions. As a result, both polarizations can excite the TM polarized PhPs, which can be measured by the electron.

The TM polarization of the PhPs means that they can only be excited by dipoles perpendicular to the edge. That is, assuming a linear polarizability α and a circular boundary, the induced dipole along the edge is written as $\boldsymbol{p}_{\mathrm{in}} = \alpha[(\boldsymbol{E}_{\mathrm{in}}(\phi, R, z=0)\cdot\hat{\boldsymbol{r}})\hat{\boldsymbol{r}} + (\boldsymbol{E}_{\mathrm{in}}(\phi, R, z=0)\cdot\hat{\boldsymbol{z}})\hat{\boldsymbol{z}}\,]$.Here the electric field is written in cylindrical coordinates, where R is the radius of our sample, and ϕ is the azimuthal angle. We can rewrite the induced dipole at each angle ϕ along the edges of our sample as:

$$\boldsymbol{p} \propto e^{-i\frac{\omega}{c}(\sin(\theta)\cos(\varphi)R\cdot\cos\phi+\sin(\theta)\sin(\varphi)R\cdot\sin\phi)}\cdot \left\{\begin{array}{c}\cos(\alpha)\,[\sin(\varphi)\cos\phi\,\hat{r} - \cos(\varphi)\sin\phi\,\hat{\mathrm{r}}] + \\ + e^{i\beta}\sin(\alpha)\,[\cos(\theta)\sin(\varphi)\sin\phi\,\hat{\mathrm{r}} + \cos(\theta)\cos(\varphi)\cos\phi\,\hat{\mathrm{r}} + \sin(\theta)\,\hat{\boldsymbol{z}}]\end{array}\right\}. \quad (2)$$

Next, we connect the induced dipoles and the PhP electric field produced in the sample. For a set of dipoles, this connection is done using the Dyadic Green's function $\overleftrightarrow{G}$, through:

$$\boldsymbol{E}_{\mathrm{php}}(\boldsymbol{r};\omega) = \int \mathrm{d}\boldsymbol{r}_{\boldsymbol{s}}\overleftrightarrow{G}(\boldsymbol{r};\boldsymbol{r}_{\boldsymbol{s}};\omega)\boldsymbol{p}_{\mathrm{in}}(\boldsymbol{r}_{\boldsymbol{s}};\omega)\,. \quad (3)$$

For an infinite slab, the Green's function component that excites E_z takes the form of

$$G_{zx}^{\inf}(x, y, z = 0, x_s, y_s, z' = 0; \omega)$$

$$= \frac{ic^2}{8\pi^2\omega^2}\int_{-\infty}^{\infty}\int_{-\infty}^{\infty} dq_x\, dq_y q_x e^{-iq_y(y-y_s)} e^{-iq_x(x-x_s)} r_p(q, \omega)$$

$$G_{zy}^{\inf}(x, y, z = 0, x_s, y_s, z' = 0; \omega)$$

$$= \frac{ic^2}{8\pi^2\omega^2}\int_{-\infty}^{\infty}\int_{-\infty}^{\infty} dq_x\, dq_y q_y e^{-iq_y(y-y_s)} e^{-iq_x(x-x_s)} r_p(q, \omega)$$

$$G_{zz}^{\inf}(x, y, z = 0, x_s, y_s, z' = 0; \omega)$$

$$= \frac{ic^2}{8\pi^2\omega^2}\int_{-\infty}^{\infty}\int_{-\infty}^{\infty} dq_x\, dq_y \frac{q^2}{k_z} e^{-iq_y(y-y_s)} e^{-iq_x(x-x_s)} r_p(q, \omega)$$

where c is the speed of light in vacuum and $k_z = \sqrt{\frac{\omega^2}{c^2} - q^2}$. The p-polarized reflection coefficient of the hBN slab $r_p(q, \omega)$ is a function of the in-plane momentum $q = \sqrt{q_x^2 + q_y^2}$ and the frequency ω, incorporating the PhP dispersion (shown in Fig. 3 of the main text). These Green's functions convert the dispersion in momentum space to spatial responses. The assumption of scattering boundary condition implies that the resulting interference pattern is achieved by summing up the contributions of many dipoles along the surface without considering reflections.

The analysis described here was used to generate the simulated results in Fig.1 of the main text. For simplicity our simulation approximated the boundary conditions to be scattering, rather than mixed scattering-reflecting. Nevertheless, the simulation captures the general shape and features of the wave-pattern in the experiment and is used to illustrate the basic principles of the underlying physics.

3 Coherent amplification in FERI: calculation of the amplification factor

In this section, we derive the contrast amplification formulas for PINEM and FERI. We start from the quantum electron regime, where the energy spread of the electron is significantly smaller than the light quanta ($\sigma_E \ll \hbar\omega$) such that we approximate the electron energy distribution to be a delta function centered around the initial electron energy E_0. We consider a total interaction g that is composed of a reference interaction and a sample interaction such that $g = g_s + g_r$. The energy distribution of the electron is thus given by the typical PINEM formula:

$$P(E) = \sum_n J_n^2(2|g|)\delta(E - E_0 - n\hbar\omega)\,. \tag{4}$$

We then filter the electron energy such that the signal contains only electrons that have energy higher than E_{filter}. In this case, the signal per electron is given by:

$$\text{Signal} = \sum_{n \text{ s.t. } E_0 + n\hbar\omega > E_{\text{filter}}} J_n^2(2|g|)\,. \tag{5}$$

When the ZLP of the electron is wide the amplitude of the electron should be convoluted with a Gaussian. However, in the "classical ensemble" regime where the incoherent broadening of the electron is wider than the photon quanta, all the interferences arising from the different Bessel functions wash out and we can convolve the probability density with the ZLP width instead of the amplitude (*1*). In this case, if the electron energy spread is given by ΔE, the final energy spectrum is given by:

$$P(E) = \sum_n \frac{1}{\sqrt{2\pi}\Delta E} J_n^2(2|g|) e^{-\frac{(E - E_0 - n\hbar\omega)^2}{2\Delta E^2}}\,. \tag{6}$$

The signal is filtered such that only electrons with energy greater than E_{filter} are accounted for. The filtered signal per electron is then calculated by integrating over the energy probability density:

$$\frac{1}{2}-\frac{1}{2}\cdot\sum_{n=-\infty}^{\infty}J_n^2(2|g|)\cdot\operatorname{erf}\left(\frac{E_{\text{filter}}-n\cdot\hbar\omega}{\sqrt{2}\Delta E}\right). \quad (7)$$

Below the saturation zone of PINEM (*1*) *the* signal increases with g. We assume that the maximum field on the sample results when the interaction strength $g=g_s$, and the minimum field results when the interaction strength $g=0$. In this case, the contrast in conventional PINEM is given by the difference between the signal with $g=g_s$ and $g=0$:

$$\text{Contrast}_{\text{PINEM}}=\frac{1}{2}\sum_{n=-\infty}^{\infty}[J_n^2(0)-J_n^2(2|g|)]\cdot. \quad (8)$$

In FERI the interaction strength is given by $g=g_r+g_s$. To exemplify the enhancement, we compare the situation when there is no field on the sample ($|g|=|g_r|$) and the case where the sample field and the reference field constructively interfere $|g|=|g_r|+|g_s|$. In this case, the contrast given in a FERI experiment is:

$$\text{Contrast}_{\text{FERI}}=\frac{1}{2}\sum_{n=-\infty}^{\infty}\left[J_n^2(2|g_r|)-J_n^2\big(2(|g_r|+|g_s|)\big)\right]\cdot\operatorname{erf}\left(\frac{E_{\text{filter}}-E_0-n\cdot\hbar\omega}{\sqrt{2}\Delta E}\right). \quad (9)$$

By dividing the two contrast formulas we can get the total amplification formula presented in the methods section:

$$\text{Amplification}=\frac{\sum_{n=-\infty}^{\infty}\left[J_n^2(2|g_r|)-J_n^2\big(2(|g_r|+|g_s|)\big)\right]\cdot\operatorname{erf}\left(\frac{E_{\text{filter}}-E_0-n\cdot\hbar\omega}{\sqrt{2}\Delta E}\right)}{\sum_{n=-\infty}^{\infty}[J_n^2(0)-J_n^2(2|g|)]\cdot\operatorname{erf}\left(\frac{E_{\text{filter}}-E_0-n\cdot\hbar\omega}{\sqrt{2}\Delta E}\right)}. \quad (10)$$

To understand the formula better it is valuable to look at the behavior in the limit of $|g_s| \ll 1$. We look separately and the denominator and numerator and Taylor expand them to the lowest non-vanishing order. In this case the denominator reads:

$$|g_s|^2 \cdot \left[2\,\mathrm{erf}\left(\frac{E_{\mathrm{filter}} - E_0}{\sqrt{2}\Delta E}\right) - \mathrm{erf}\left(\frac{E_{\mathrm{filter}} - E_0 - \hbar\omega}{\sqrt{2}\Delta E}\right) - \mathrm{erf}\left(\frac{E_{\mathrm{filter}} - E_0 + \hbar\omega}{\sqrt{2}\Delta E}\right)\right]. \quad (11)$$

While the numerator reads:

$$\sum_n 2|g_s| \cdot J_n(2|g_r|)\left(J_{n-1}(2|g_r|) - J_{n+1}(2|g_r|)\right) \cdot \mathrm{erf}\left(\frac{E_{\mathrm{filter}} - E_0 - n \cdot \hbar\omega}{\sqrt{2}\Delta E}\right). \quad (12)$$

The critical part here is that the numerator scales linearly with $|g_s|$ while the denominator scales quadratically. This shows us how the interferometric information give rise to $\frac{1}{|g_s|}$ amplification for weak fields, this amplification is the core of the improved imaging sensitivity we present in this work.

4 Laser and phase stability characterization

In this section, we present additional characterizations performed during this work to estimate the phase stability and to quantify the laser's spectral and temporal properties. We also show that the reference laser phase and amplitude distribution is approximately uniform across the electron beam, justifying our approximation of a uniform reference.

To test the stability of our electron interferometer, we operated our setup as a Michelson interferometer at 780 nm (Fig. S1). We acquired approximately 50 interference measurements with experimental parameters similar to those used in the presented experiment. These stability measurements were taken at two different delays, and we measured their corresponding phases. The standard deviation of the phase in the visible regime was approximately 0.6 radians, providing a good characterization of the mechanical stability of our electron interferometer. Given that the driving wavelength in the mid-infrared is approximately ten times longer than in

the visible range, the standard deviation of the phase translates to 60 milliradians for the electron interferometer in the presented hBN measurements, or 240 as uncertainty in the cycle.

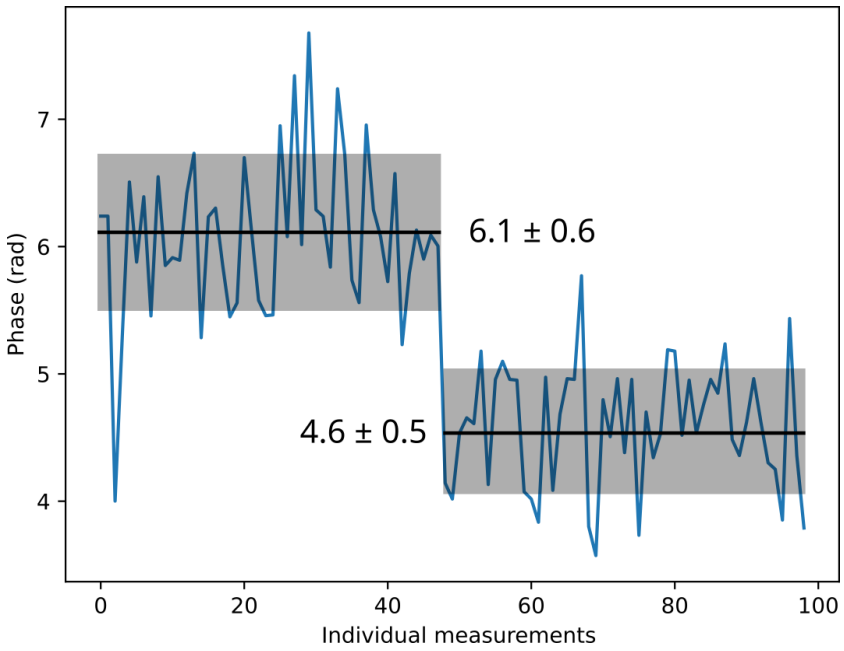

Fig. S1 | Phase stability measurement of the delay stage using a Michelson interferometer at 780 nm. We estimate a ~0.6 radian noise, tested at two arbitrary delays for comparison. This noise translates to ~0.06 radians noise for the mid-IR frequencies used in this work.

Additionally, we examined the periodicity of the phase measurements. The most straightforward method involved conducting an EELS scan with modulated electrons on an hBN sample. Our findings reveal an average period of 23.3 fs in EELS, which corresponds to a wavelength of 7 microns, consistent with the driving laser used in the experiment. The results are presented in Fig. S2.

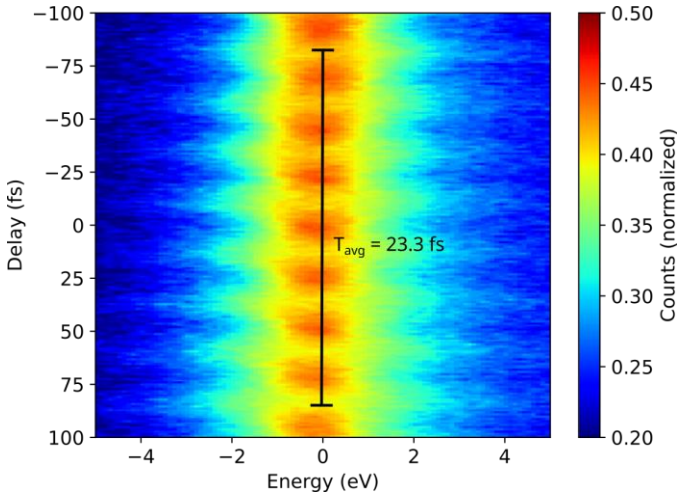

Fig. S2 | Periodicity of the interference measurement. To test the stability of the interferometer, we measure the EELS spectrum of the sample plus reference interaction as a function of the relative delays and observe a stable periodicity.

In our reconstruction, we assumed that the electron phase prior to the sample interaction is spatially uniform. This assumption is justified due to the large laser spot on the reference aluminum mirror (~100 microns radius), which is much larger than the electron beam spot size (~6 microns radius). To quantify this spatial uniformity, we perform additional measurements with two flat aluminum mirrors, one as the reference, and one as the sample. We then measure the energy-filtered electron counts as a function of delay between the stages and see periodic oscillation of the electron measurement with a spot that remains spatially uniform on a scale of 20 microns, which is larger than the electron spot size used in the experiment. The results are presented in Fig. S3.

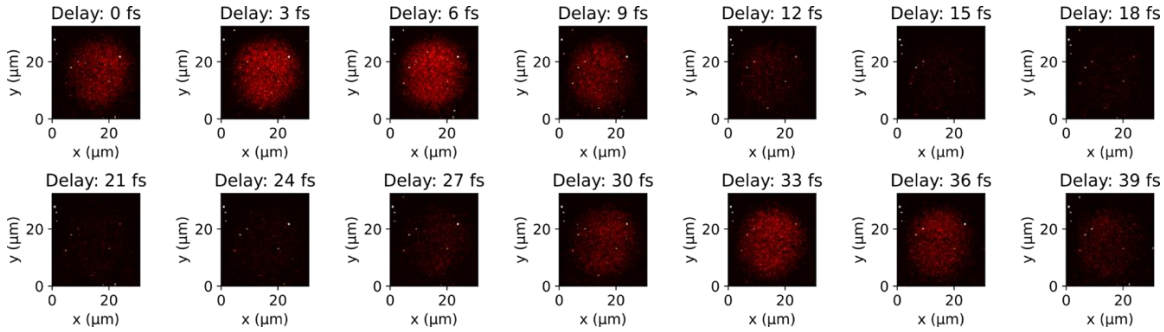

Fig. S3 | Amplitude and phase homogeneity in the transverse plane. We measure the energy-filtered electron counts as a function of delay between interactions with two flat aluminum mirrors. The data shows the periodicity, as well as the homogeneity of the image over a transverse area of $\sim 20x20\mu\mathrm{m}^2$. This observation indicates a homogenous reference interaction in both amplitude and phase for the other measurements in our work.

To measure the temporal profile of the exciting laser, we performed electron energy spectrum measurement with a flat aluminum mirror (see Fig. S4a). A known result for PINEM (*2*) is that post PINEM interaction, the variance of the electron energy distribution is $\Delta E^2_{\mathrm{final}} = \Delta E^2_{\mathrm{initial}} + (\hbar\omega g)^2$, where $\Delta E^2_{\mathrm{initial}}$ is the variance of the electron energy distribution prior to the interaction. Since g is proportional to the electric field, by measuring the electron variance as a function of time delay, it is possible to reconstruct the laser intensity temporal profile (with temporal resolution comparable to the electron pulse duration, hundreds of fs).

Fig. S4b presents the temporal profile of the pump pulse, as measured by this method. The multi-peaked form of the pulse is due to its propagation through the atmosphere, which caused substantial dispersion, creating a few sharp sub-pulses with roughly 1ps duration. The effect of the first two sub-pulses can be seen in Fig. 2 in the main text, where the second sub-pulse is seen exciting the edge of the sample near the end of the simulation (at around 1.5 ps). The first sub-pulse creates the polariton wavepacket presented in the manuscript, and we can see it already propagating significantly from the edge before the **s**econd sub-pulse arrives.

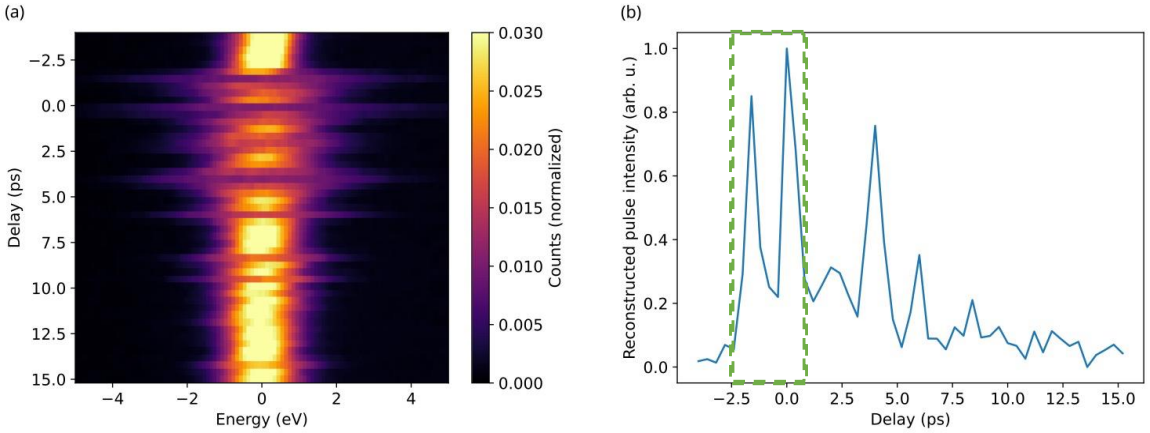

Fig. S4 | Measuring the temporal profile of the laser pulse. We measure the energy filtered electron counts as a function of delay between interactions with two flat aluminum mirrors. The green frame marks the range of times used for Fig.2 in the main text. We see that a second pulse arrives ~1.5 ps after the first one, as is also seen in panel Fig.2b2.

We present the pulse spectrum for each of the central wavelengths used in Fig. 3 of the manuscript.

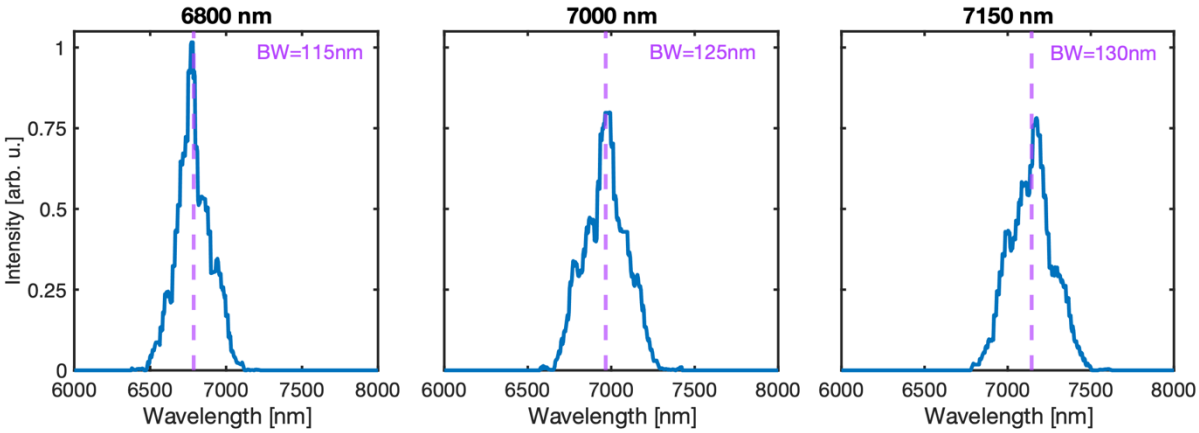

Fig. S5 | Measurements of the spectra of the laser pulse, showing the tunability over the range of wavelengths relevant for excitation of the hBN phonon-polaritons.

SI References

[1] Y. Pan, B. Zhang, A. Gover, Anomalous Photon-Induced Near-Field Electron Microscopy. *Phys. Rev. Lett.* **122**, 183204 (2019).

[2] O. Reinhardt, I. Kaminer, Theory of Shaping Electron Wavepackets with Light. *ACS Photonics*. **7**, 2859–2870 (2020).

Movie captions SM1-SM2: Phonon-polariton PINEM delay-scan in the hBN micro-drum. Each frame of these movies corresponds to an energy-filtered electron image. The delay between the laser pulse impinging on the sample and the electron probe pulse is increased for each frame by 10 fs (50 fs) for movie SM1 (SM2). This allows one to construct the time evolution of the phonon polariton dynamics, showcasing the "hopping" effect as discussed in the main manuscript.

Movie captions SM3-SM5: FERI phase-scans of phonon-polaritons in the hBN micro-drum. Each frame of these movies corresponds to an energy-filtered electron image. Each movie (SM3-SM5) is a scan over the sample-reference relative phase for $g_{\mathrm{s,max}} = 0.4, 0.8, 1.4$ using sub-cycle delay steps, allowing one to reconstruct the phase of the field at the sample. The reconstruction is based on the FERI optimization expression discussed in the methods chapter.

Other Supporting Information for this manuscript include the following:
Movies SM1 to SM5